# A MIMETIC FINITE VOLUME METHOD ON COLLOCATED GRIDS FOR INCOMPRESSIBLE FLOWS

## D. Santos, J.A. Hopman, J. Plana and F.X. Trias

## Heat and Mass Transfer Technological Center - Technical University of Catalonia

daniel.santos.serrano@upc.edu

#### **Abstract**

We propose a mimetic finite volume method (FVM) on collocated grids tailored for incompressible flow simulations, with an emphasis on symmetry preservation and numerical stability. The methodology is grounded in a rigorous framework of Reduction and Reconstruction operators, ensuring consistent discretization of integral quantities. By formulating discrete differential operators using geometric and topological mappings, the proposed approach naturally extends to complex physical models such as magnetohydrodynamics (MHD). A symmetry-preserving and unconditionally stable projection method is derived, minimizing spurious kinetic energy production commonly introduced in collocated formulations. The method is validated through a benchmark problem involving 2D buoyant flow in the presence of a strong magnetic field, where numerical results show excellent agreement with analytical solutions while enabling efficient resolution of thin boundary layers with high-aspect ratio, non-uniform meshes. When compared with the results reported by Elisabet et al. (2011), our method achieves higher accuracy using a mesh that is approximately eight times smaller, underscoring the efficiency and precision of the proposed formulation.

#### 1 Introduction

Several widely used CFD solvers—such as Open-FOAM and Fluent—employ a collocated FVM layout due to its simplicity, adaptability to unstructured meshes, and suitability for handling complex geometries (see Trias et al., 2014; Fig. 1). Despite these advantages, collocated arrangements come with well-documented drawbacks when compared to staggered grids (e.g., Verstappen and Veldman, 2003). Notably, issues such as checkerboarding of pressure fields (Hopman et al., 2025) and numerical instabilities (Santos et al., 2025) can arise.

To address checkerboarding, a Compact Laplacian scheme is often applied. While effective, this approach introduces spurious contributions to the kinetic energy balance, which may compromise simulation stability. In contrast, staggered grid methods can preserve kinetic energy by construction, provided the discretization respects the inherent symmetries of the differential operators (Verstappen and Veldman, 2003).

However, even with symmetry-preserving schemes, collocated formulations that solve a compact Poisson equation for pressure may still introduce artificial energy through the pressure-velocity coupling. This remains a key challenge when designing robust collocated solvers for high-fidelity simulations.

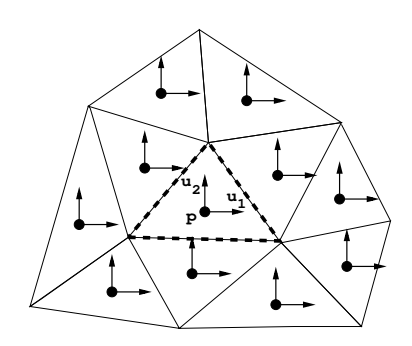


Figure 1: General collocated arrangement.

In practice, stability issues in numerical simulations are often addressed by modifying interpolation schemes or refining the computational mesh until the instabilities disappear. While sometimes effective, this trial-and-error approach can be inefficient, leading to unnecessary computational cost and time consumption. Instead, this work aims to adopt a more principled perspective by revisiting the foundations of the FVM. Specifically, it seeks to bridge the gap between discrete numerical schemes and classical vector calculus formulations, with a focus on identifying the origin of artificial kinetic energy errors and proposing a consistent remedy.

The FVM, like many numerical methods, follows a structured process: it begins by integrating the governing differential equations to obtain conserved (integral) quantities over control volumes. These integrals are then approximated discretely, yielding a solvable algebraic system. Finally, the discrete solution—defined at a finite number of degrees of freedom—is extended over the entire domain using some form of interpolation or reconstruction.

This procedure can be systematically understood using two conceptual mappings: the Reduction operator  $\mathcal R$  which projects continuous fields onto integral quantities (e.g., fluxes or cell averages), and the Reconstruction operator  $\mathcal I$  which lifts the discrete solu-

tion back into a continuous field over the domain. Figure 2 illustrates this reduction–reconstruction framework, which provides a formal structure for analyzing and improving the consistency and stability of FVM schemes.

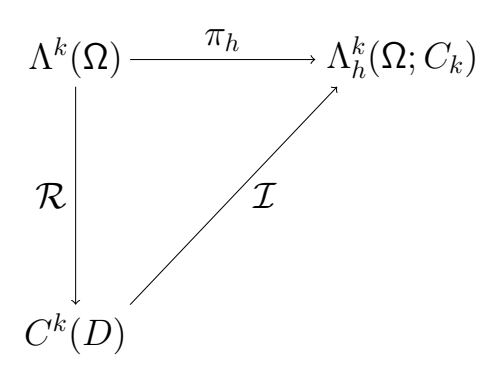


Figure 2: Diagram illustrating the Reduction  $\mathcal{R}$  and Reconstruction  $\mathcal{I}$  maps.

The  $\Lambda^k(\Omega)$  space is the space of continuous variables,  $C^k(D)$  is the space of integrated quantities, and  $\Lambda^k_h(\Omega; C_k)$  is the space of reconstructed variables. The superindex k indicates if the quantity is related to points (k=0), to lines (k=1), to surfaces (k=2) or to volumes (k=3).

#### 2 Reduction and Reconstruction maps

The Reduction and Reconstruction maps need to satisfy the following properties:

- 1.  $\mathcal{RI} = id$  (consistency property).
- 2.  $IR = id + O(h^s)$  (approximation property).

It may happen that  $\Lambda_h^k(\Omega; C_k) \notin \Lambda^k(\Omega)$ . This is the case for non-continuous Reconstructions, such as FVM or Discontinuous Galerkin methods.

Consider a field  $\Phi^{(3)}$ , defined over volumes. Its integral over a control volume  $\Omega_i$  defines the action of  $\mathcal{R}$ , which yields a discrete representation of the field:

$$\int_{\Omega_i} \Phi^{(3)} dV \approx \Phi_i V_i \implies \mathcal{R}\Phi^{(3)} = \Phi_i V_i, \quad (1)$$

where the integral is approximated using the Mid Point integral rule, as is common in FVM. Here,  $\Phi_i$  represents the value of the field at the center of control volume i, and  $V_i$  is its volume.

In a similar fashion, for quantities defined on faces—such as a surface flux  $u^{(2)}$ —the Reduction map for 2-forms can be expressed as:

$$\int_{f} u^{(2)} \mathbf{dS} \approx \mathbf{u}_{f} \cdot \mathbf{n}_{f} S_{f} \implies$$

$$\mathcal{R}u^{(2)} = \mathbf{u}_{f} \cdot \mathbf{n}_{f} S_{f}, \tag{2}$$

where the integral is approximated using the midpoint rule, consistent with standard FV practices. Here,  $\mathbf{u}_f$  is the vector velocity at the face center,  $\mathbf{n}_f$  is the outward

unit normal vector to the face and  $S_f$  is the surface of the face f.

To complete the formulation, we define the Reconstruction operator  $\mathcal{I}$ , which must fulfill both consistency and approximation properties. In the context of FVM, a simple and commonly used reconstruction is the piecewise constant reconstruction:

$$\mathcal{I}(\phi_i V_i) = \phi_i \mathbb{1}_{\Omega_i}(\mathbf{x}),\tag{3}$$

where  $\mathbb{1}_{\Omega_i}$  is is the indicator function for cells, equal to 1 if  $x \in \Omega_i$  and 0 otherwise. Extending this reconstruction to the entire computational domain yields:

$$\mathcal{IR}\Phi^{(3)} = \sum_{i} \phi_{i} \mathbb{1}_{\Omega_{i}}(\mathbf{x}). \tag{4}$$

This results in a discontinuous field, where the value is uniform inside each cell but may jump across cell interfaces. To recover values at the cell faces—required, for instance, in flux computations—interpolation schemes are applied in FVM.

#### 3 Discretizing operators

It is important to highlight that the Reduction map can be used to construct discrete counterparts of continuous differential operators. Consider, for example, the divergence of a surface-associated vector field  $u^{(2)}$ :

$$\mathcal{R}(\nabla \cdot u^{(2)}) = \int_{V_i} \nabla \cdot u^{(2)} dV = \int_{\partial V_i} u^{(2)} \mathbf{dS}$$

$$\implies \sum_{f \in \partial V_i} \int_f u^{(2)} \mathbf{dS} = \sum_{f \in \partial V_i} \mathcal{R}_f u^{(2)}, \quad (5)$$

where  $\mathcal{R}_f u^{(2)}$  denotes the Reduction of  $u^{(2)}$  over face f. This formulation naturally decouples the geometric and topological aspects of the divergence operator: the Reduction  $\mathcal{R}$  encapsulates the geometric integration, while the summation over faces corresponds to the topological structure of the mesh.

This summation can be expressed using an incidence matrix  $\delta$ , which encodes the connectivity between faces and control volumes. Using this matrix, the discrete divergence operator is compactly written as:

$$\mathcal{R}(\nabla \cdot u^{(2)}) = \delta \mathcal{R} u^{(2)}. \tag{6}$$

We define the  $L^2$ -inner product as

$$(\Phi^{(k)}, \Psi^{(k)})_{\Omega} := \int_{\Omega} \langle \Phi^{(k)}, \Psi^{(k)} \rangle dV, \tag{7}$$

where  $\langle \cdot, \cdot \rangle$  denotes the pointwise scalar product. This formulation enables us to define the metric of the collocated space:

$$\int_{\Omega} \langle \Phi^{(k)}, \Psi^{(k)} \rangle dV = \sum_{i} \Phi_{i} V_{i} \Psi_{i} \implies (\Phi^{(k)}, \Psi^{(k)})_{\Omega} = \Phi_{c}^{T} \Omega_{c} \Psi_{c}, \tag{8}$$

where  $\Phi_c$  and  $\Psi_c$  are vectors containing the discrete values of  $\Phi^{(k)}$  and  $\Psi^{(k)}$  at the cell centers, and  $\Omega_c$  is a diagonal matrix containing the collocated volumes on its diagonal.

If the fields are vector-valued and include components x, y and z, then the inner product extends to:

$$(\Phi^{(k)}, \Psi^{(k)})_{\Omega} = \Phi_c^T \Omega \Psi_c, \tag{9}$$

where  $\Omega = \mathbb{I}_3 \otimes \Omega_c$  and  $\mathbb{I}_3$  is the  $3 \times 3$  identity matrix. In the context of the  $L^2$ -inner, the Hilbert adjoint of the divergence operator is the gradient. Applying this property to the reconstructed forms yields:

$$(\mathcal{I}(\delta \mathcal{R}u^{(2)}), \Phi^{(3)})_{\Omega} = (u^{(2)}, -\mathsf{G}\Phi^{(3)})_{\Omega_s} \Longrightarrow \mathsf{G} = -\Omega_s^{-1}\mathsf{M}^T, (10)$$

where  $M = \delta \mathcal{R}$  is the reduced divergence and  $\Omega_s$  is a diagonal matrix containing the staggered volumes on its diagonal.

Using this discrete gradient, the (compact) Laplacian operator can then be defined as:

$$L = MG. \tag{11}$$

providing a symmetric and structure-preserving formulation suitable for collocated finite volume schemes.

### 4 Discretization of the Incompressible Navier-Stokes Equations on Collocated Grids

Consider a computational domain composed of n control volumes and m faces. The discretized incompressible Navier–Stokes equations in collocated form can be written as:

$$\Omega \frac{d\mathbf{u}_{c}}{dt} + C(\mathbf{u}_{s}) \mathbf{u}_{c} + D\mathbf{u}_{c} + \Omega G_{c} \mathbf{p}_{c}$$

$$= \mathbf{0}_{c}, \quad (12a)$$

$$M\mathbf{u}_s = \mathbf{0}_c, \qquad (12b)$$

where  $\mathbf{p}_c = (p_1, p_2, \dots, p_n)^T \in \mathbb{R}^n$  and  $\mathbf{u}_c \in \mathbb{R}^{3n}$  are the cell-centered pressure and collocated velocity fields, respectively. The subindices c and s indicate if the variables are cell-centered or staggered at the faces.

To ensure mass conservation in each control volume, the velocity field at faces is introduced as  $\mathbf{u}_s = \left((u_s)_1, (u_s)_2, (u_s)_3, \dots, (u_s)_m\right)^T \in \mathbb{R}^m$ , and linked to cell-centered quantities via a cell-to-face interpolation operator:

$$\Gamma_{c \to s} = N(\mathsf{I}_3 \otimes \Pi_{c \to s}),\tag{13}$$

where  $\Pi_{c \to s} \in \mathbb{R}^{m \times n}$  is the scalar cell-to-face interpolator, and  $N = (N_{s,x}N_{s,y}N_{s,z}) \in \mathbb{R}^{3m \times m}$ , where  $N_{s,i} \in \mathbb{R}^{m \times m}$  is a diagonal matrix containing the  $x_i$  spatial components of the face normal vectors.

The matrices  $\Omega \in \mathbb{R}^{3n \times 3n}$ ,  $C(\mathbf{u}_s) \in \mathbb{R}^{3n \times 3n}$  and  $D \in \mathbb{R}^{3n \times 3n}$  are block diagonal matrices given by

$$\Omega = I_3 \otimes \Omega_c$$
,  $C(\mathbf{u}_s) = I_3 \otimes C_c(\mathbf{u}_s)$ ,  $D = I_3 \otimes D_c$ ,

where  $I_3 \in \mathbb{R}^{3 \times 3}$  is the identity matrix and  $\Omega_c \in \mathbb{R}^{n \times n}$  is a diagonal matrix containing the cell-centered control volumes.  $C_c(\mathbf{u}_s) \in \mathbb{R}^{n \times n}$  and  $D_c \in \mathbb{R}^{n \times n}$  are the cell-centered convective and diffusive operators for a discrete scalar field, respectively. Finally,  $G_c \in \mathbb{R}^{3n \times n}$  is the discrete gradient operator, and the matrix  $M \in \mathbb{R}^{n \times m}$  is the face-to-center discrete divergence operator.

When applying projection-based methods—such as PISO or the Fractional Step Method (FSM)—to decouple pressure and velocity in the discretized Navier—Stokes equations, stability is not always guaranteed, especially when a Compact Poisson operator is employed. In explicit time integration schemes, an additional (artificial) kinetic energy contribution is introduced by the pressure gradient. This spurious energy term can be expressed as (Santos et al., 2025):

$$\mathbf{p}_c^T(\mathsf{L} - \mathsf{L}_c)\mathbf{p}_c,\tag{14}$$

where L denotes the Compact Laplacian and  $L_c$  denotes the Wide-Stencil Laplacian.

The conditions that the discretization must satisfy to ensure numerical stability are stated in the following theorem (Santos et al., 2025):

**Theorem** Assumptions:

- Our projection method adds a kinetic energy error of the form p<sup>T</sup><sub>c</sub>(L - L<sub>c</sub>)p<sup>T</sup><sub>c</sub> (such as the FSM or PISO).
- The method preserves the symmetries of the differential operators.

Then,  $\mathbf{p}_c^T(\mathsf{L}-\mathsf{L}_c)\mathbf{p}_c^T \leq 0$  at each time step  $\iff$ 

1. The volume-weighted interpolator is used for the pressure gradient.

2.

$$V_k = \sum_{f \in F(k)} \tilde{V}_{k,f} n_{i,f}^2, \ \forall k \in \{1, ..., n\},$$

$$\sum_{f \in F(k)} \tilde{V}_{k,f} n_{i,f} n_{j,f} = 0, \ \forall k \in \{1, ..., n\},$$

where  $\tilde{V}_{k,f} = \delta_{k,f} S_f$ , where  $\delta_{k,f}$  is the projected distance between the cell center and the face. The volume-weighted interpolator is an interpolation that conserves integrated quantities when interpolating from cells to faces and can be constructed in any mesh as follows:

$$\Pi_{c \to s} = \Delta_s^{-1} \Delta_{sc}^T, \tag{15}$$

where  $\Delta_s \in \mathbb{R}^{m \times m}$  is a diagonal matrix containing the projected distances between two adjacent control volumes, and  $\Delta_{sc} \in \mathbb{R}^{m \times n}$  is a matrix containing the projected distances between an adjacent cell node and its corresponding face. Fig.3 shows a representation of these distances.

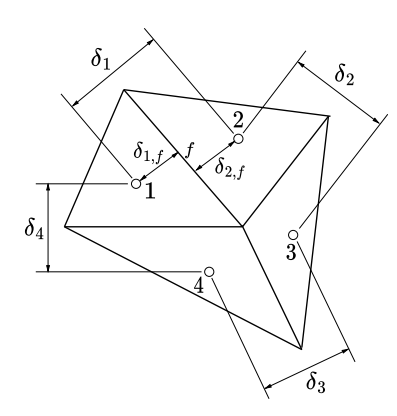


Figure 3:  $\delta_i$  are the components of  $\Delta_s$ , while the components of  $\Delta_{sc}$  would be calculated in the same way but taking the distance between a control volume and their corresponding face centers.

## Discretization of the Magnetohydrodynamic equations in the quasi-static approximation

In the regime of low magnetic Reynolds number Rm, also referred to as the quasi-static approximation, the influence of the fluid motion on the magnetic field is negligible. Under this assumption, the magnetic field remains externally imposed and unaltered by the flow dynamics. Consequently, the governing equations for thermal MHD buoyant flow can be conveniently formulated using the electric potential  $\phi$ .

$$\frac{\partial \mathbf{u}}{\partial t} + (\mathbf{u} \cdot \nabla)\mathbf{u} = -\frac{\nabla p}{\rho} + \nu \nabla^2 \mathbf{u}$$

$$+ \frac{\mathbf{j} \times \mathbf{B}_0}{\rho} + \mathbf{g}\beta (T - T_{ref}), \qquad (16a)$$

$$\nabla \cdot \mathbf{u} = 0, \qquad (16b)$$

$$\mathbf{j} = \sigma_m (-\nabla \phi + \mathbf{u} \times \mathbf{B}_0)(16c)$$

$$\nabla \cdot \mathbf{j} = 0, \qquad (16d)$$

$$\frac{\partial T}{\partial t} = \mathbf{T}_0 (\mathbf{g}) = \mathbf{T}_0^2 \mathbf{g} = \mathbf{U}(\mathbf{s})$$

$$\frac{\partial T}{\partial t} + \nabla \cdot (\mathbf{u}T) = \alpha \nabla^2 T, \tag{16e}$$

where **u** is the velocity vector, p is the pressure,  $\rho$  is the density,  $\nu$  is the kinematic viscosity, **j** is the current density,  $\mathbf{B}_0$  is the externally applied magnetic field,  $\mathbf{g}$ is the gravity vector,  $\beta$  is the thermal expansion coefficient,  $\sigma_m$  is the electrical conductivity,  $\phi$  is the electric potential, T is the temperature,  $T_{ref}$  is the reference temperature and  $\alpha$  is the thermal diffusivity.

By combining Eqs. (16c) and (16d), a Poisson equation for the electric potential can be derived as:

$$\nabla^2 \phi = \nabla \cdot (\mathbf{u} \times \mathbf{B}_0). \tag{17}$$

All necessary discrete operators are available to numerically solve this equation. The following outlines the steps of a FSM applied to the discretized system for a fully explicit first order time integration scheme:

$$\mathbf{u}_{c}^{p} = \mathbf{u}_{c}^{n} - \Delta t \Omega^{-1} [\mathsf{C} (\mathbf{u}_{s}) + \mathsf{D}] \mathbf{u}_{c}^{n}$$

$$+ \frac{\mathbf{j}_{c}^{n} \times \mathbf{B}_{0}}{\rho} + \mathbf{g} \beta (T^{n} - T_{ref}), \qquad (18a)$$

$$\mathbf{u}_{s}^{p} = \Gamma_{c \to s} \mathbf{u}_{c}^{p}, \qquad (18b)$$

$$\mathsf{L} \mathbf{p}_{c}^{n+1} = \mathsf{M} \mathbf{u}_{s}^{p} \to \mathbf{p}_{c}^{n+1}, \qquad (18c)$$

$$\mathbf{u}_{s}^{n+1} = \mathbf{u}_{s}^{p} - \mathsf{G} \mathbf{p}_{c}^{n+1}, \qquad (18d)$$

$$\mathbf{u}_{c}^{n+1} = \mathbf{u}_{c}^{p} - \Gamma_{s \to c} \mathsf{G} \mathbf{p}_{c}^{n+1}, \qquad (18e)$$

$$\mathbf{j}_{s}^{p} = \mathbf{u}_{s}^{n} \times \mathbf{p}_{c}^{p} \qquad (18f)$$

$$\mathbf{u}_s^p = \Gamma_{c \to s} \mathbf{u}_c^p, \tag{18b}$$

$$\mathsf{L}\mathbf{p}_{c}^{n+1} = \mathsf{M}\mathbf{u}_{s}^{p} \to \mathbf{p}_{c}^{n+1}, \tag{18c}$$

$$\mathbf{u}_s^{n+1} = \mathbf{u}_s^p - \mathsf{G}\mathbf{p}_c^{n+1}, \tag{18d}$$

$$\mathbf{u}_c^{n+1} = \mathbf{u}_c^p - \Gamma_{s \to c} \mathsf{G} \mathbf{p}_c^{n+1}, \tag{18e}$$

$$\mathbf{j}_c^p = \mathbf{u}_c^n \times \mathbf{B}_0, \tag{18f}$$

$$\mathbf{j}_{s}^{p} = \Gamma_{c \to s} \mathbf{j}_{c}^{p}, \tag{18g}$$

$$\mathbf{j}_{s}^{p} = \Gamma_{c \to s} \mathbf{j}_{c}^{p}, \qquad (18g)$$

$$\mathsf{L}\phi^{n+1} = \mathsf{M}\mathbf{j}_{s}^{p}, \to \phi_{c}^{n+1} \qquad (18h)$$

$$\mathbf{j}_{c}^{n+1} = \sigma_{m} \Gamma_{s \to c} (\mathbf{j}_{s}^{p} - \mathsf{G} \phi^{n+1}), \quad (18i)$$

$$T^{n+1} = T^{n} + \Delta t (-\mathsf{C}(\mathbf{u}_{s}) + \alpha \mathsf{L}) T^{n} (18j)$$

$$T^{n+1} = T^n + \Delta t(-C(\mathbf{u}_s) + \alpha L)T^n (18i)$$

The implemented solver is an extension based on the Runge-Kutta symmetry-preserving solver found in https://github.com/janneshopman/RKSymFoam.

It is important to emphasize that for the solver to remain unconditionally stable, the interpolator  $\Gamma_{c\to s}$ must be the volume-weighted (Santos et al., 2025). Additionally, the operator  $\Gamma_{s\to c}$  must satisfy the following condition (Trias et al., 2014)):

$$\Gamma_{s \to c} = \Omega^{-1} \Gamma_{c \to s}^T \Omega_s. \tag{19}$$

## Numerical test: 2D Buoyant flow in an enclosure in the presence of a strong horizontal magnetic field

The proposed method is particularly well-suited for scenarios where mesh refinement is required only in localized regions—such as boundary layers—while a coarser mesh suffices elsewhere. Its unconditional stability, even in the presence of high aspect ratios between adjacent control volumes, enables the use of meshes with significant size variations.

This is especially advantageous in MHD, where fine resolution is typically needed near the walls to capture boundary layer effects, while the core (bulk) region can be discretized more coarsely. In such cases, the boundary layer-known as the Hadamard layer-scales inversely with the Hartmann number, defined as  $Ha = B_0 L \sqrt{\frac{\sigma_m}{\mu}}$ , where  $B_0$  is the external magnetic field, L is a characteristic length,  $\sigma_m$  is the electrical conductivity and  $\mu$  is the dynamic viscosity. It is important to note that as the strength of the external magnetic field increases, the Hartmann number also rises, resulting in a thinner boundary layer.

The test case involves a two-dimensional buoyancy-driven cavity flow with electrically conductive walls and a strong horizontal magnetic field applied perpendicular to the temperature gradient, as illustrated in Fig.4 (Tagawa et al., 2002). An analytical solution for the gradient of the transversal velocity W at the center of the plane is available for this configuration, providing a valuable benchmark for validation.

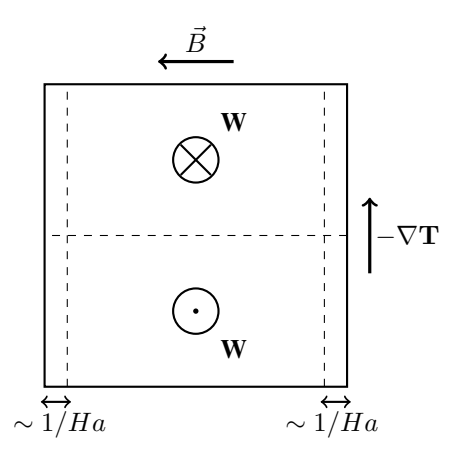


Figure 4: 2D enclosed buoyant cavity with conductive walls full of liquid metal with a strong horizontal magnetic field. Hadamard boundary layers are also depicted.

A test case with a Hartmann number of Ha=500 has been selected for analysis. Multiple mesh configurations were tested, two of which are shown in Fig.5 and Fig.6. In these meshes, only six control volumes are placed in the bulk (along the direction of the magnetic field), while 27 control volumes are concentrated near each boundary wall.

The mesh identification convention is illustrated in Fig.5: a label like (90–10;10–90;1) indicates that 90% of the domain contains only 10% of the total control volumes, with a uniform aspect ratio of 1. Conversely, the remaining 10% near the wall contains 90% of the cells, with an aspect ratio of 10 between the smallest and largest control volumes. The aspect ratio between bulk and wall control volumes of this mesh is 37.5.

Similarly, the mesh shown in Fig.6 is labeled as (97-3;10-90;10), meaning that 97% of the domain contains just 10% of the control volumes, and the boundary layer (3% of the domain) is resolved using 90% of the control volumes with an aspect ratio of 10. The aspect ratio between bulk and wall control volumes of this mesh is 108.

We begin by estimating the thickness of the Hadamard boundary layer using the mesh shown in Fig.5, where the refined region is positioned near the wall at x=-0.045m. After running the simulation, the boundary layer thickness was determined to be approximately 0.015m (see Fig.7). Based on this result, a new mesh with finer resolution near the boundary was developed, as shown in Fig.6.

Table 1 shows a comparison of the obtained value for dW/dX at the center of the plane against the analytical value:

As anticipated, Case C (Fig.6) outperforms Case A (Fig.5) in terms of accuracy. Case B demonstrates that even a slight increase in the boundary layer mesh thickness can degrade the solution quality. Moreover, Cases C, D, and E reveal that, beyond just refining the

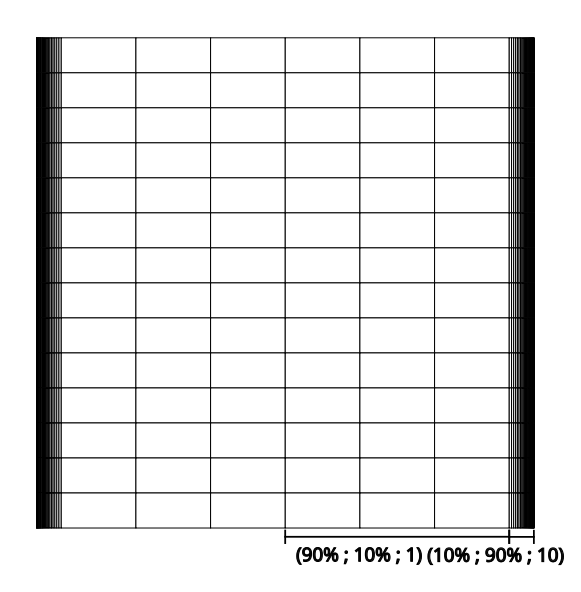


Figure 5: Test mesh (90-10;10-90;10). The aspect ratio between the bulk and the wall control volumes is 37.5.

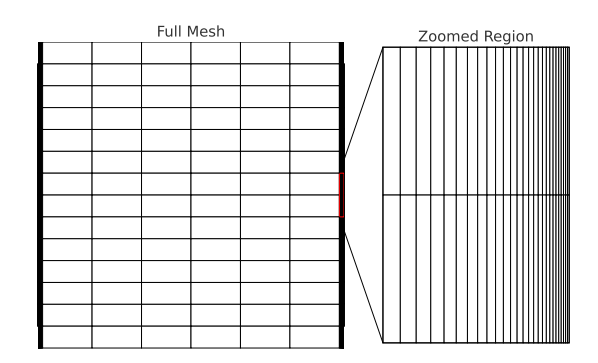


Figure 6: Test mesh (97-3;10-90;10). A zoomed region is shown close to the wall. The aspect ratio between the bulk and the wall control volumes is 108.

Ha = 500	Mesh	Analytical: 10.00
15x60 (A)	(90-10; 10-90; 10)	10.10
15x60 (B)	(96-4; 10-90; 10)	10.03
15x60 (C)	(97-3; 10-90; 10)	10.02
15x60 (D)	(97-3; 10-90; 4)	10.03
15x60 (E)	(97-3; 10-90; 2)	10.05
15x60 (F)	(97-3; 10-90; 1)	10.09
15x30 (G)	(97-3; 10-90; 10)	10.07
15x30 (H)	(97-3; 10-90; 20)	10.05

Table 1: Comparison of numerical results of dW/dX at the center of the plane for Ha = 500 for different meshes.

boundary layer, positioning the first node as close as possible to the wall improves accuracy. Lastly, Cases G and H compare results from a 15x30 mesh to those from a 15x60 mesh. The comparison between Case G and Case A clearly shows that strategically placing control volumes near critical regions is more effective than simply increasing mesh density in the bulk.

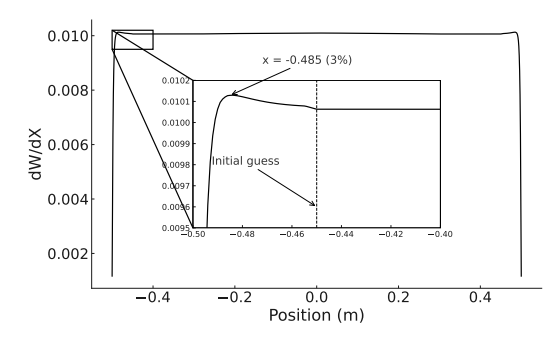


Figure 7: Plot of dW/dX with the position. The initial estimate for the boundary layer thickness was  $0.05\,\mathrm{m}$ , while the simulation results indicate a refined value of approximately  $0.015\,\mathrm{m}$ .

A comparison with the work of Elisabet et al. (2011) shows that our method attains higher accuracy using a significantly coarser mesh—eight times smaller in size.

#### 7 Conclusions

This work introduces a mimetic finite volume method on collocated grids that preserves the structural properties of the governing equations, particularly for incompressible and MHD flows. The core of the methodology relies on consistent Reduction and Reconstruction operators, enabling the derivation of discrete operators that closely mimic their continuous counterparts. A key contribution is the development of a symmetry-preserving projection method that ensures unconditional stability—even on high-aspect ratio meshes—.

The method was successfully applied to a canonical MHD benchmark problem involving buoyancy-driven flow in a 2D cavity with an imposed magnetic field. Results demonstrate that strategic mesh refinement near boundaries (rather than uniform refinement) yields higher accuracy and efficiency. Notably, placing the first node as close as possible to the wall and ensuring proper interpolation across cell interfaces were shown to be critical for achieving accurate gradient estimations. In particular, compared to the results of Elisabet et al. (2011), the proposed approach delivers improved accuracy with a mesh that is eight times smaller, highlighting the method's superior efficiency and suitability for boundary layer-dominated problems.

These findings establish a foundation for extending mimetic and structure-preserving FVM strategies to more complex flows and multiphysics scenarios on general unstructured grids.

#### Acknowledgments

This work is supported by the SIMEX project (PID2022-142174OB-I00) of *Ministerio de Ciencia e Innovación*, Spain. D. Santos acknowledges a *FI AGAUR-Generalitat de Catalunya* fellowship (2022FI\_B\_00173), extended and financed by *Universitat Politècnica de Catalunya and Banc Santander*. J.A.H. is supported by the predoctoral grant FI 2023 (2023 FI\_B1 00204) of the *Catalan Agency for Management of University and Research Grants (AGAUR)*. J.P is supported by a *FI AGAUR-Generalitat de Catalunya* fellowship (2022FI\_B\_00810).

#### References

Hopman, J.A., Santos, D., Alsalti-Baldellou, À., Rigola, J. and Trias F.X. (2025), Quantifying the checkerboard problem to reduce numerical dissipation, *J. Comp. Phys.*, Vol. 521, 113537.

Mas de les Valls E., Batet L., de Medina V.,Fradera J. and Sedano L. (2011), Modelling of integrated effect of volumetric heating and magnetic field on tritium transport in a U-bend flow as applied to HCLL blanket concept, *Fusion Eng. Des.*, Vol. 86 pp. 341-356.

Santos. D., Hopman, J.A., Pérez-Segarra, C.D., and Trias F.X. (2025), On a symmetry-preserving unconditionally stable projection method on collocated unstructured grids for incompressible flows, *J. Comp. Phys.*, Vol. 523, 113631.

Tagawa, T., Authié, G. and Moreau, R. (2002), Buoyant flow in long vertical enclosures in the presence of a strong horizontal magnetic field. Part 1. Fully-established flow, *Eur. J. Mech. B Fluids*, Vol. 21, pp. 383–398.

Trias, F.X., Lehmkuhl, O., Oliva, A., Pérez-Segarra, C.D. and Verstappen, R.W.C.P. (2014), Symmetry-preserving discretization of Navier-Stokes equations on collocated unstructured meshes, *J. Comp. Phys.*, Vol. 258, pp. 246-267.

Verstappen, R.W.C.P. and Veldman, A.E.P. (2003), Symmetry-preserving discretization of turbulent flow, *J. Comp. Phys.*, Vol. 187, pp. 343-368.